

# Exploring Diffusion with Test-Time Training on Efficient Image Restoration

Rongchang Lu<sup>2</sup>, Tianduo Luo<sup>1</sup>, Yunzhi Zhang<sup>1</sup>, Conghan Yue<sup>3</sup>, Pei Yang<sup>1,\*</sup>,  
Guibao Liu<sup>1</sup> and Changyang Gu<sup>1</sup>

<sup>1</sup> Department of Computer Technology and Applications, Qinghai University, 810016, Xining China

<sup>2</sup> School of Ecological and Environmental Engineering, Qinghai University, Xining, 810016, China

<sup>3</sup> School of Computer Science, Sun Yat-sen University, Guangzhou 510006, China

\* Correspondence Author: 2016990018@qhu.edu.cn

**Abstract.** Image restoration faces challenges including ineffective feature fusion, computational bottlenecks and inefficient diffusion processes. To address these, we propose **DiffRWKVIR**, a novel framework unifying Test-Time Training (TTT) with efficient diffusion. Our approach introduces three key innovations: (1) *Omni-Scale 2D State Evolution* extends RWKV's location-dependent parameterization to hierarchical multi-directional 2D scanning, enabling global contextual awareness with linear complexity  $\mathcal{O}(L)$ ; (2) *Chunk-Optimized Flash Processing* accelerates intra-chunk parallelism by  $3.2\times$  via contiguous chunk processing ( $\mathcal{O}(LCd)$  complexity), reducing sequential dependencies and computational overhead; (3) *Prior-Guided Efficient Diffusion* extracts a compact Image Prior Representation (IPR) in only 5-20 steps, proving 45% faster training/inference than DiffIR while solving computational inefficiency in denoising. Evaluated across super-resolution and inpainting benchmarks (Set5, Set14, BSD100, Urban100, Places365), DiffRWKVIR outperforms SwinIR, HAT, and MambaIR/v2 in PSNR, SSIM, LPIPS, and efficiency metrics. Our method establishes a new paradigm for adaptive, high-efficiency image restoration with optimized hardware utilization.

**Keywords:** Image Restoration · Super-Resolution · Diffusion Model · RWKV · Test-Time Training.

## 1 Introduction

Image restoration (IR) addresses the reconstruction of high-quality images from degraded inputs, with super-resolution and inpainting representing its fundamental tasks. Traditional IR techniques, such as bicubic or B-spline[5] methods, often produce blurry results with compromised details, whereas modern deep learning approaches have demonstrated remarkable success in preserving spatial and spectral information through sophisticated architectures. Significant advancements include Convolutional Neural Networks (CNNs) [24][23] which play a pivotal

role in advancing image restoration by utilizing residual connections and multi-scale learning to aggregate local features effectively. Further improvements are achieved through attention mechanisms that capture long-range dependencies to refine feature representations, along with State-Space Modeling (SSM)-based methods[6] such as State-Space 2D (SS2D)[20] which introduce linear attention for efficient sequential modeling, thereby achieving superior computational scalability and performance. Moreover, the DiffIR model[11] adopts diffusion models (DMs)[2] as an iterative generative process[8] to progressively denoise images from Gaussian noise to recover high-fidelity outputs.

**Table 1.** Computational complexity and parallelism comparison.

Model	FLOPs	Steps	Parallelism
SwinIR[21], HAT[22], DiffIR[11]	$O(L^2d)$	1	Full
MambaIR[20]/v2[1]	$O(Ld^2)$	$L$	None
DiffRWKVIR(Ours)	$O(LCd)$	$L/C$	Chunk-wise

Despite the significant success of image restoration models[8][39][40], distinct hierarchical structures in certain imagery challenge conventional methods: (1) **Ineffective feature fusion** occurs as CNNs have limited receptive fields, Transformers incur quadratic costs with local cross-shaped attention, and state-space models (SSMs)[6] like Mamba suffer from edge blurring and artifacts. (2) **High computational overhead** persists: Transformer-based super-resolution models exhibit quadratic complexity, while linear attention[7] and SSM-based methods[6] are hampered by sequential processing and poor memory access patterns. As Table 1 shows, SwinIR[21]/HAT[22] ( $O(L^2d)$ ) require global parallelism but incur high FLOPs, MambaIR[20] variants ( $O(Ld^2)$ ) need  $L$  sequential steps with no parallelism, and our approach achieves efficient chunk-wise parallelism.

We propose **DiffRWKVIR** with three innovations: (1) **Omni-Scale 2D State Evolution**, which is inspired by Receptance Weighted Key Value (RWKV)[17, 18, 4, 19] and enables global contextual awareness via hierarchical branches and location-dependent parameterization with linear complexity, (2) **Chunk-Optimized Flash Processing** that reduces computational overhead through contiguous chunk processing inspired by Flash Linear Attention mechanism[3], achieving  $3.2\times$  faster intra-chunk parallelism ( $O(LCd)$  complexity,  $L/C$  chunks in Table 1, (3) **Prior-Guided Efficient Diffusion** which is initially encouraged by DiffIR[11] but proposed work proves 45% less training and inference time than DiffIR, and solves the computational inefficiency of conventional diffusion models by extracting critical Image Prior Representation (IPR) in merely 5-20 steps.

## 2 Preliminaries and Proposed Mechanisms

This work introduces a novel framework that synergizes Test-Time Training (TTT) with Denoising Diffusion Probabilistic Models (DDPMs) to address dynamic degradation challenges in image super-resolution. The integration enables

real-time adaptation to unseen distortions during inference while leveraging DDPM’s hierarchical feature learning for spatial dependency modeling. This section formalizes the core components and their theoretical foundations.

## 2.1 Denoising Diffusion Probabilistic Models

Denoising Diffusion Probabilistic Models (DDPMs) establish the probabilistic foundation for hierarchical feature learning through two interconnected Markov processes. The forward diffusion process systematically corrupts data by incrementally adding Gaussian noise across  $T$  steps. This degradation follows the transition kernel

$$q(\mathbf{x}_t | \mathbf{x}_{t-1}) = \mathcal{N}(\mathbf{x}_t; \sqrt{1 - \beta_t} \mathbf{x}_{t-1}, \beta_t \mathbf{I}), \quad (1)$$

where  $\beta_t$  controls the noise schedule. As  $t$  approaches  $T$ , the data  $\mathbf{x}_T$  converges to isotropic Gaussian noise, dissolving all original structure. The reverse process aims to reconstruct the original data by learning a parameterized denoising trajectory. It iteratively refines  $\mathbf{x}_t$  back to  $\mathbf{x}_0$  using the conditional distribution:

$$p_\theta(\mathbf{x}_{t-1} | \mathbf{x}_t) = \mathcal{N}(\mathbf{x}_{t-1}; \mu_\theta(\mathbf{x}_t, t), \Sigma_\theta(\mathbf{x}_t, t)), \quad (2)$$

where  $\mu_\theta$  and  $\Sigma_\theta$  are predicted by a neural network trained to reverse the diffusion steps.

## 2.2 State Evolution and Theoretical Formulation

The proposed State Evolution mechanism is based on Test-Time Training (TTT), which enables dynamic parameter adaptation during inference, overcoming the static limitation of conventional deep learning models. By continuously refining parameters through self-supervised learning, TTT compresses historical context  $\{\mathbf{x}_i\}_{i=1}^T$  into a latent state  $\mathbf{S}_t$  that parameterizes a trainable model  $\mathcal{F}$ . The  $\mathbf{S}_t$  evolves via the output prediction  $\mathbf{y}_t = \mathcal{F}(\mathbf{x}_t; \mathbf{S}_t)$  via gradient-based optimization:

$$\mathbf{S}_t = \mathbf{S}_{t-1} - \eta \nabla_{\mathbf{S}} \mathcal{L}(\mathbf{S}_{t-1}; \mathbf{x}_t). \quad (3)$$

Here,  $\mathcal{L}$  denotes a self-supervised loss (e.g., reconstruction error), and  $\eta$  controls the adaptation rate. Building on this, the proposed linear attention mechanism establishes an efficient input-output mapping via state weight  $\mathbf{S}_t$  and the loss  $\mathcal{L} = \frac{1}{2} \|\mathbf{y}_t - \mathbf{x}_t \mathbf{S}_{t-1}^T\|_2^2$ . The gradient derivation yields:

$$\frac{\partial \mathcal{L}}{\partial \mathbf{S}_{t-1}} = \mathbf{S}_{t-1} \mathbf{x}_t^T \mathbf{x}_t - \mathbf{y}_t^T \mathbf{x}_t, \quad (4)$$

resulting in the compact update:

$$\mathbf{S}_t = \mathbf{S}_{t-1} (\omega - \mathbf{x}_t^T \mathbf{x}_t \eta) + \mathbf{y}_t^T \mathbf{x}_t \eta. \quad (5)$$

This combines TTT’s adaptability with error-driven plasticity while maintaining  $\mathcal{O}(L)$  complexity.

### 2.3 2D State Evolution Module

Standard state evolution processes data causally, ignoring non-local spatial dependencies in images. To address this, we extend the mechanism to 2D via multi-directional scanning (Fig. 1), capturing forward, backward, upward, and downward semantics.

This fusion enables simultaneous learning of high-level abstractions and low-level spatial details, bridging sequential adaptation with image-specific requirements.

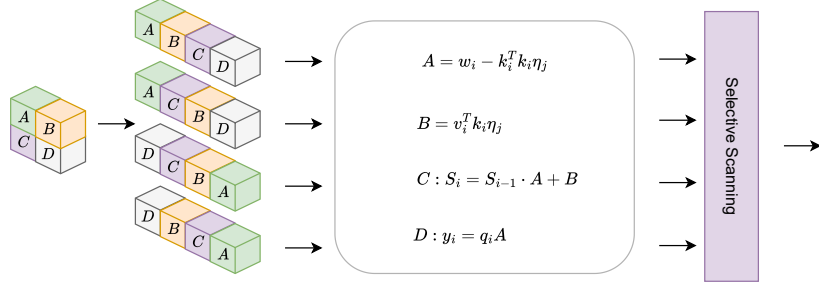


**Fig. 1.** 2D State Evolution Mechanism

### 2.4 Chunk-wise Iteration Acceleration

To mitigate computational overhead, we adopt chunk-wise processing inspired by Flash Linear Attention. Input  $\mathbf{X} \in \mathbf{R}^{L \times d}$  is divided into  $N = \lceil L/C \rceil$  chunks of size  $C$ . Using the *WY representation* for Householder matrices, the state updates as:

$$\mathbf{S}_{t+1} = \mathbf{S}_t + \underbrace{(\mathbf{U}_t - \mathbf{W}_t \mathbf{S}_t^\top) \mathbf{K}_t}_{\Delta \mathbf{S}_t}, \quad (6)$$

where  $\mathbf{U}_t, \mathbf{W}_t$  derive from the *UT transform*:

$$\mathbf{T}_t = (\mathbf{I} + \text{tril}(\text{diag}(\beta_t) \mathbf{K}_t \mathbf{K}_t^\top, -1))^{-1} \text{diag}(\beta_t). \quad (7)$$

Chunk outputs combine inherited states and intra-chunk attention, reducing sequential dependency from  $O(L)$  to  $O(d)$  while preserving theoretical advantages:

$$\mathbf{O}_t = \mathbf{Q}_t \mathbf{S}_t^\top + \underbrace{(\mathbf{Q}_t \mathbf{K}_t^\top \odot \mathbf{M}_C)}_{\text{intra-chunk}} \mathbf{U}_t. \quad (8)$$

This allows efficient computation of pseudo-values  $\mathbf{U}_t = \mathbf{T}_t \mathbf{V}_t$  and weight updates  $\mathbf{W}_t = \mathbf{T}_t \mathbf{K}_t$  entirely through batched matrix multiplications.

### 3 Methodology

#### 3.1 Model Architecture

The proposed DiffRWKVIR framework employs a two-stage architecture following DiffIR to address the fundamental challenges in image restoration. Stage 1 focuses on compact prior extraction using a U-Net backbone, while Stage 2 implements efficient prior-guided restoration through an enhanced diffusion mechanism.

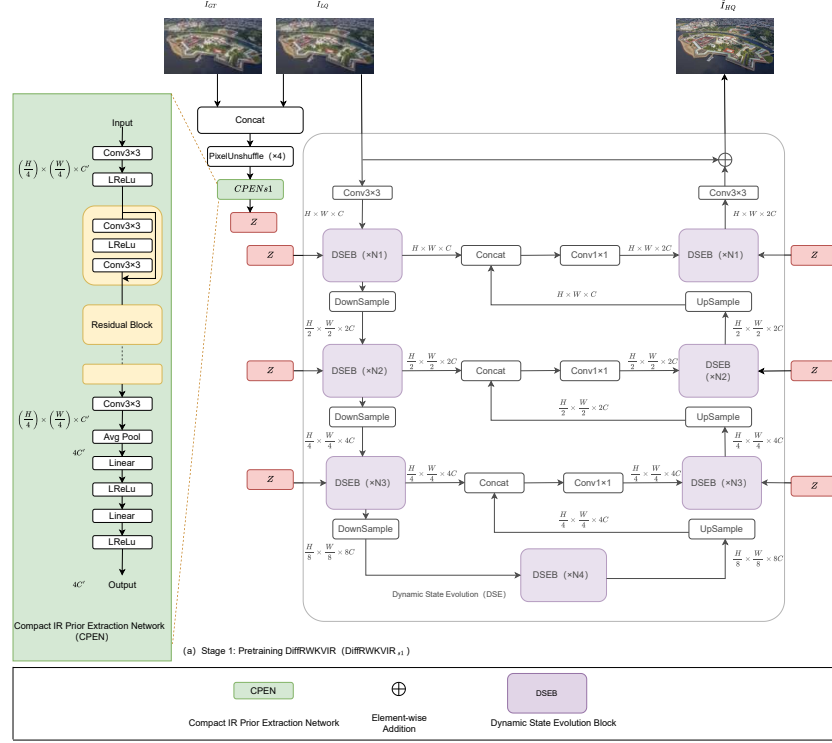


**Fig. 2.** The stage 1 architecture of our proposed DiffRWKVIR.

**Stage 1: Compact Prior Extraction ( $\text{DiffRWKVIR}_{s1}$ ):** As illustrated in Fig. 2, this stage implements a U-Net structured Compact IR Prior Extraction Network (CPEN). The network processes input image  $\mathbf{I}$  through convolutional layers and residual blocks, employing PixelUnshuffle for resolution adjustment. The core innovation is the integration of Dynamic State Evolution Blocks (DSE-Blocks) within the encoding and decoding paths. Each DSE block implements the update mechanism:

$$\mathbf{S}_t = \mathbf{S}_{t-1}(\omega - \mathbf{x}_t^\top \mathbf{x}_t \eta) + \mathbf{y}_t^\top \mathbf{x}_t \eta \quad (9)$$

where  $\mathbf{S}_t$  represents the evolving state tensor. These blocks alternate with Channel Attention Blocks (CAB) and residual connections, enabling multi-scale feature fusion. This stage outputs a compact Image Prior Representation (IPR)  $\mathbf{Z}$  that encodes hierarchical features across scales.

**Stage 2: Prior-Guided Restoration (DiffRWKVIR<sub>s2</sub>):** As depicted in Fig. 3, Stage 2 implements an efficient diffusion process conditioned on the IPR. During training, low-quality  $\mathbf{I}_{LQ}$  and ground-truth  $\mathbf{I}_{GT}$  images are concatenated and processed through PixelUnshuffle ( $\times 4$ ) and CPE<sub>ns1</sub> to extract feature  $\mathbf{Z}$ . The state evolution provides spatial context while the IPR guides the restoration of spectral details, which enables high-fidelity reconstruction with dramatically fewer diffusion steps than conventional DDPMs.

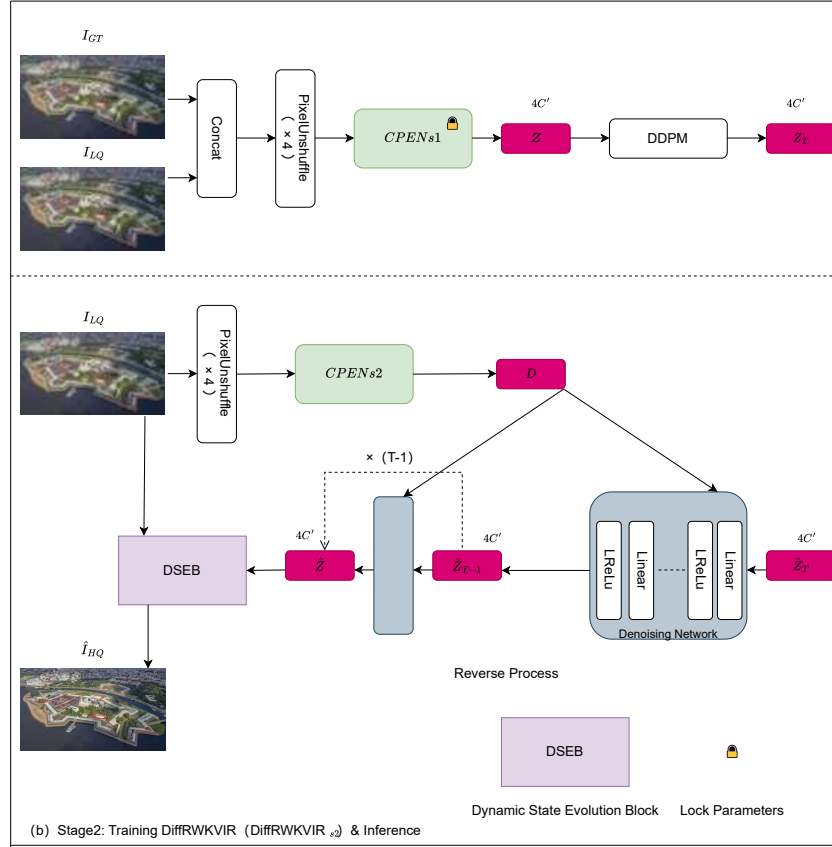


**Fig. 3.** The stage 2 architecture of our proposed DiffRWKVIR.

### 3.2 Dynamic State Evolution Block

The Dynamic State Evolution Block (DSEB) constitutes the core computational unit of the Dynamic-ESR framework, integrating the State Evolution Block (SEB) and Channel Attention Block (CAB) into a unified architecture. Crucially, the CAB functions as the Feed Forward Network within this block, while the SEB incorporates the Omni-Shift mechanism for comprehensive spatial modeling. This design enables dynamic feature evolution with linear complexity while preserving multi-scale spatial relationships.

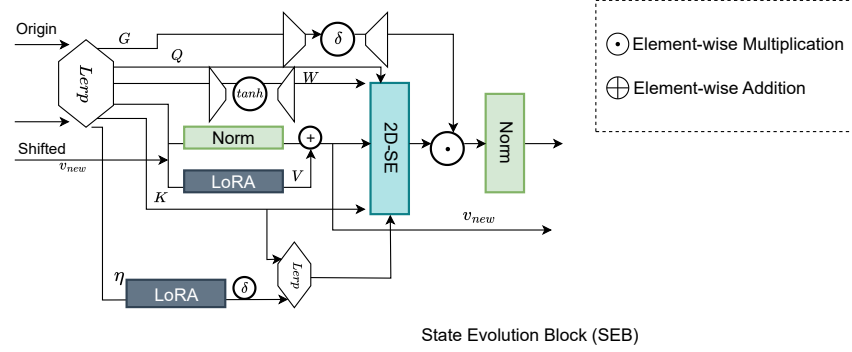


**Fig. 4.** Structure of SEB, which is a component of the DSEB.

The SEB processes input  $\mathbf{x} \in \mathbb{R}^{B \times T \times C}$  through token shift operations that capture adjacent semantics, as shown in Fig. 4. Key components  $\mathbf{q}$ ,  $\mathbf{w}$ ,  $\mathbf{k}$ ,  $\mathbf{v}$ , and  $\eta$  are derived via learnable weights with Softplus activation for dynamic adjustment, followed by Low-Rank Adaptation (LoRA) and Linear Interpolation (LeRP) transformations that generate intermediate representations:

$$\text{LoRA}(\mathbf{x}) = \mathbf{A} \text{Tanh}(\mathbf{x} \mathbf{B}), \text{LeRP}(\mathbf{a}, \mathbf{b}) = \mathbf{a} + (\mathbf{b} - \mathbf{a}) \odot \mu. \quad (10)$$

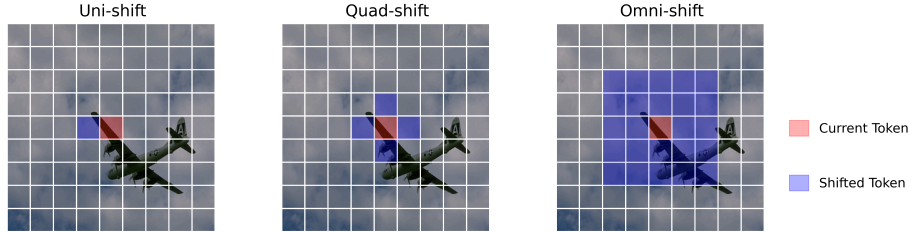


**Fig. 5.** Illustrated Comparison of Uni-Shift, Quad-Shift and Omni-Shift.

The Omni-Shift module in SEB, as shown in Fig. 6, enhances spatial modeling through multi-scale convolutional fusion. This multi-scale processing enables more hierarchical feature fusion while maintaining 2D structural relationships, compared to uniform directional shift (Uni-Shift) and quad-directional

shift (Quad-Shift) in Fig. 5. The final 2D State Evolution (2DSE) output combines these components through layer normalization and projection, with residual connections preserving feature integrity.

As the Feed Forward Network component, the CAB, as shown in Fig. 7, operates on feature maps  $F \in \mathbf{R}^{C \times H \times W}$  through channel-wise recalibration:

$$F_{\text{output}} = F \odot \sigma(W_2 \cdot \text{ReLU}(W_1 \cdot \text{GlobalAveragePooling}(F))). \quad (11)$$

This residual connections ensure gradient stability and feature preservation throughout processing, as shown in Fig. 8. The integrated architecture dynamically adjusts feature representations through learnable states, enabling robust adaptation to varying input conditions while maintaining computational efficiency.

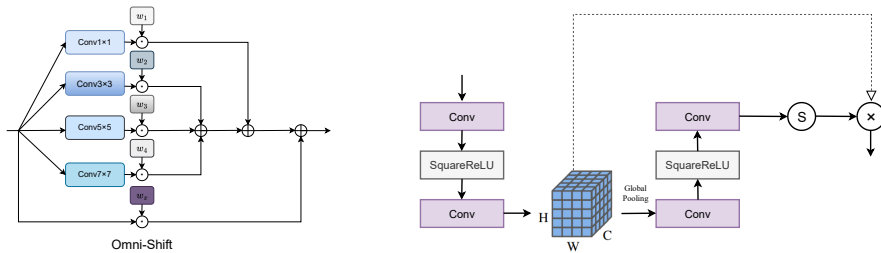


**Fig. 6.** Illustration of Omni-Shift

**Fig. 7.** Structure of CAB

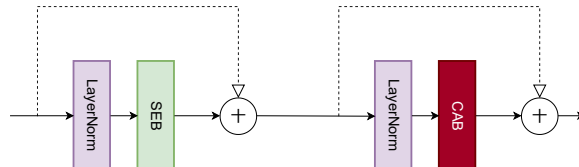


**Fig. 8.** Structure of DSEB

## 4 Experimental Setup

### 4.1 Datasets and Implementation Details

The DF2K[31][34] dataset (3,450 high-resolution images from DIV2K[31] and Flickr2K[34]) serves as our training foundation. We generate low-resolution counterparts via bicubic downscaling to  $48 \times 48$  patches, with corresponding HR patches scaled to  $96 \times 96$  ( $2 \times$ ) and  $192 \times 192$  ( $4 \times$ ) for multi-scale training. Validation uses 800 DIV2K[31] images, while evaluation employs standard benchmarks: Set5[32], Set14[28], BSD100[33], and Urban100[29]. Implemented in PyTorch on NVIDIA A100 GPUs, models are trained with random  $48 \times 48$  LR crops, rotation

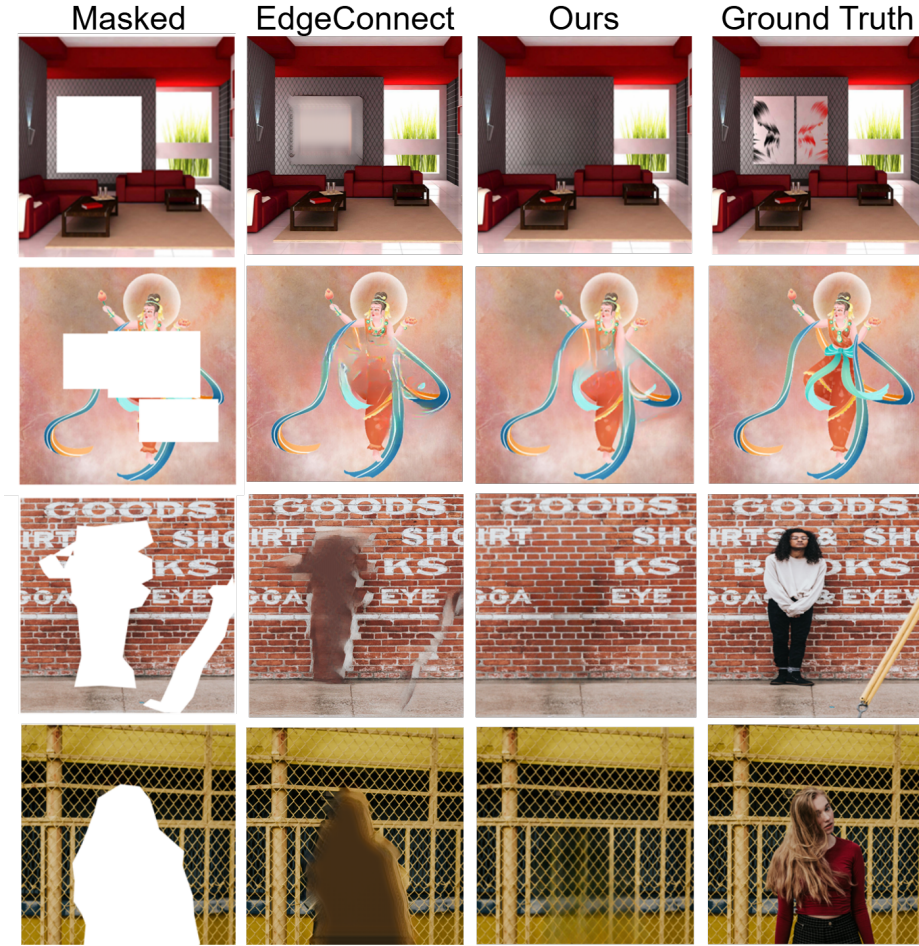
augmentation, batch size 16, and Adam optimization ( $\beta_1 = 0.9$ ,  $\beta_2 = 0.99$ ). The learning rate initiates at  $1 \times 10^{-4}$  with  $10 \times$  decay after 80 epochs. Architecturally, we incorporate 4 residual groups containing 6 residual blocks each. Performance assessment employs complementary task-specific metrics: super-resolution evaluation utilizes PSNR and SSIM [35] for spatial fidelity, RMSE for pixel error, SAM for spectral consistency, LPIPS [38] for perceptual similarity, and NIQE [37] for non-reference naturalness, while inpainting tasks are evaluated using PSNR, SSIM [35], LPIPS [38], and FID [36] to measure reconstruction quality and distribution alignment.

## 4.2 Results

Quantitative evaluations comprehensively demonstrate the superior performance of our DiffRWKVIR framework across diverse image restoration benchmarks.

For image inpainting, DiffRWKVIR achieves remarkable performance improvements across three challenging datasets: Places365, Celeba-HQ, and Mural. As illustrated qualitatively in Fig. 9, our approach generates visually coherent completions with significantly reduced artifacts and perceptual distortions compared to existing methods. Quantitatively, we observe substantial gains in both fidelity and perceptual metrics as shown in Table 2. For example, on Places365, we achieve a 0.53 dB PSNR improvement over the previous state-of-the-art while simultaneously enhancing SSIM by 2.18% and reducing FID by 0.7%.

In super-resolution tasks, DiffRWKVIR consistently surpasses all evaluated baselines—including transformer-based (SwinIR, HAT), SSM-based (MambaIR/v2), and diffusion-based (DiffIR) approaches—across all five benchmark datasets at  $\times 4$  magnification scales. As comprehensively detailed in Table 3, our method demonstrates particular advantages in perceptual quality metrics while maintaining superior pixel-level accuracy. For example, on Urban100, which contains challenging urban structures, we achieve a 0.025 dB PSNR gain and 0.36% SSIM improvement while reducing LPIPS by 3.9% compared to DiffIR. Qualitative comparisons provide compelling visual evidence of DiffRWKVIR’s superiority, particularly in reconstructing high-frequency details and complex textures. As shown in Fig. 10, our method produces significantly sharper and more natural reconstructions compared to existing approaches.

**Fig. 9.** Qualitative Result on inpainting tasks**Table 2.** Quantitative comparison results for inpainting on benchmark datasets. The best and second-best performance are marked in bold and underlined.

Dataset	Method	PSNR $\uparrow$	SSIM $\uparrow$	LPIPS $\downarrow$	FID $\downarrow$
Places365	ICT[13]	22.26	0.8813	0.1302	2.1110
	EdgeConnect[16]	21.16	0.7312	0.1367	2.3213
	LDM[14]	22.35	0.8706	0.1440	2.1512
	AOT-GAN[15]	21.65	0.7734	0.1398	6.8933
	Lama[12]	<u>22.37</u>	<u>0.8750</u>	0.1353	2.2777
	DiffIR[11]	22.35	0.8744	<b>0.1167</b>	<b>1.1210</b>
	DiffRWKVIR(Ours)	<b>22.88</b>	<b>0.8962</b>	<u>0.1207</u>	<u>1.1283</u>
Celeba-HQ	ICT[13]	22.43	0.7760	0.1296	9.8794
	EdgeConnect[16]	22.84	0.7994	0.1247	8.9133
	LDM[14]	23.61	0.8448	0.1136	<u>8.1128</u>
	AOT-GAN[15]	24.47	0.8494	0.1080	8.2175
	Lama[12]	23.46	<u>0.8880</u>	0.1124	8.3793
	DiffIR[11]	<u>24.51</u>	0.8494	<u>0.1072</u>	8.2175
	DiffRWKVIR(Ours)	<b>24.53</b>	<b>0.8887</b>	<b>0.1063</b>	<b>7.1987</b>
Mural	ICT[13]	—	—	—	—
	EdgeConnect[16]	21.16	0.7314	0.1538	<u>54.9843</u>
	LDM[14]	—	—	—	—
	AOT-GAN[15]	19.01	0.6821	0.1582	58.7557
	Lama[12]	20.77	0.8273	0.1577	62.1924
	DiffIR[11]	<u>21.72</u>	<b>0.8494</b>	<u>0.1511</u>	58.2175
	DiffRWKVIR(Ours)	<b>21.88</b>	0.8326	<b>0.1485</b>	<b>52.8218</b>

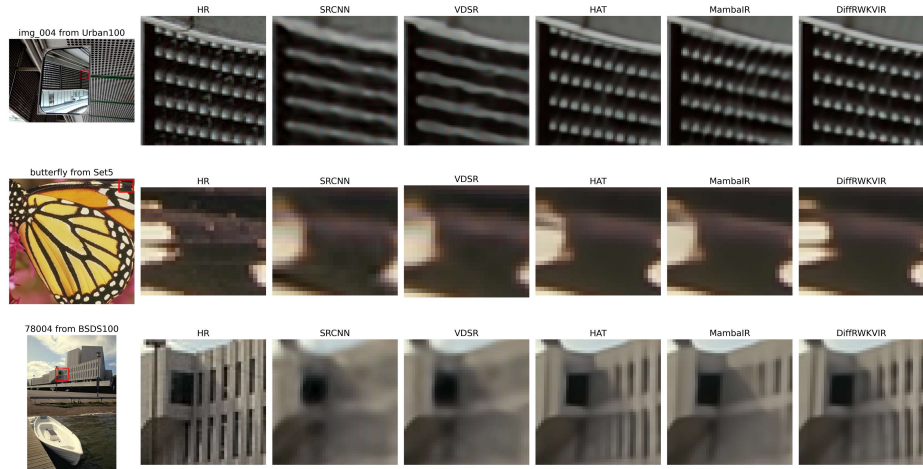


**Fig. 10.** Qualitative Results on Super-Resolution tasks

**Table 3.** Quantitative comparison results for the BSD100[33], Set14[28], Set5[32], Manga109[30] and Urban100[29] datasets (Scale  $\times 4$ ).

Dataset	Method	PSNR $\uparrow$	SSIM $\uparrow$	NIQE $\downarrow$	LPIPS $\downarrow$	RMSE $\downarrow$	SAM $\downarrow$
BSD100	SRCNN[24]	25.4822	0.6865	6.7947	0.3483	6.8053	0.179924
	VDSR[23]	25.8393	0.7030	6.8562	0.3400	6.6668	0.179922
	SwinIR[21]	26.5038	0.7443	6.1012	0.3284	6.4368	0.179907
	HAT[22]	26.5244	0.7283	6.2093	0.3242	6.4338	0.176125
	MambaIR[20]	26.3487	0.7208	6.5026	0.3411	6.5237	0.170451
	MambaIRv2[1]	26.6818	0.7337	6.2854	0.3213	6.4228	0.170305
	DiffIR[11]	<u>26.7612</u>	0.7445	<u>6.0516</u>	<u>0.3118</u>	<b>6.3767</b>	<b>0.165610</b>
Set14	Ours	<b>26.7741</b>	<b>0.7493</b>	<b>6.0509</b>	<b>0.3086</b>	<u>6.3994</u>	<u>0.165984</u>
	SRCNN[24]	26.1297	0.7274	6.8363	0.3086	6.6540	0.181809
	VDSR[23]	26.6535	0.7476	7.0664	0.2963	6.4315	0.180565
	SwinIR[21]	26.8202	0.7737	6.2152	0.2895	6.4306	0.179725
	HAT[22]	27.4404	0.7791	6.1809	0.2844	6.2429	0.179644
	MambaIR[20]	26.9452	0.7656	6.2648	0.3033	6.4020	0.179566
	MambaIRv2[1]	27.4892	0.7802	6.1319	0.2824	6.2251	0.178309
Set5	DiffIR[11]	<u>27.5345</u>	<u>0.7998</u>	<b>5.8072</b>	<u>0.2656</u>	<u>6.1978</u>	<u>0.173432</u>
	Ours	<b>27.5970</b>	<b>0.8023</b>	<u>5.8193</u>	<b>0.2635</b>	<b>6.1906</b>	<b>0.172631</b>
	SRCNN[24]	28.9618	0.8433	8.0359	0.2242	5.7970	0.174728
	VDSR[23]	29.7875	0.8669	8.8137	0.2118	5.4403	0.171906
	SwinIR[21]	30.6960	0.8890	7.1031	0.2083	5.4660	0.171485
	HAT[22]	31.1306	0.8931	7.1819	0.2037	5.1480	0.171253
	MambaIR[20]	30.5195	0.8847	7.0029	0.2135	5.2987	0.171146
Manga109	MambaIRv2[1]	31.2377	0.8937	7.1085	0.2012	<u>5.0978</u>	0.163690
	DiffIR[11]	<u>31.3076</u>	<u>0.9033</u>	<b>6.5072</b>	<b>0.1756</b>	5.1978	<b>0.153432</b>
	Ours	<b>31.3209</b>	<b>0.9241</b>	<u>6.6868</u>	<u>0.1759</u>	<b>5.0855</b>	<u>0.156567</u>
	SRCNN[24]	25.8335	0.8325	6.0457	0.2053	5.7328	0.166248
	VDSR[23]	27.0357	0.8664	5.8027	0.1800	5.2777	0.159692
	SwinIR[21]	29.7317	0.9138	5.3363	0.1532	5.7429	0.154728
	HAT[22]	30.4798	0.9205	5.2749	0.1477	4.6890	0.152925
Urban100	MambaIR[20]	29.0316	0.9040	5.2187	0.1683	5.0095	0.151611
	MambaIRv2[1]	30.6474	0.9217	5.2264	0.1440	4.6446	0.151535
	DiffIR[11]	<u>30.7676</u>	<u>0.9433</u>	<b>4.8072</b>	<u>0.1456</u>	<u>4.6478</u>	<b>0.143432</b>
	Ours	<b>30.7739</b>	<b>0.9574</b>	<u>4.8475</u>	<b>0.1119</b>	<b>4.6229</b>	<u>0.144746</u>

**Table 4.** Unified efficiency and memory characteristics comparison. DiffRWK VIR demonstrates superior hardware utilization across all metrics while maintaining competitive model size.

Model	FLOPs (G)	Training Time	Inference Time	L2 Cache Hit (%)	MemReads (GB/s)	Params (M)
DiffIR[11]	338.56	12h 23m	65m 10s	51.2	190	10.89
SwinIR[21]	304.95	10h 23m	58m 10s	41.2	210	5.78
HAT[22]	292.42	9h 26m	56m 57s	44.7	204	6.82
MambaIR[20]	261.34	8h 35m	46m 50s	48.5	164	8.87
MambaIRv2[1]	258.12	9h 01m	50m 12s	54.1	169	9.92
Ours	<b>230.78</b>	<b>6h 52m</b>	<b>36m 56s</b>	<b>83.7</b>	<b>108</b>	<b>11.04</b>

### 4.3 Efficiency and Other Studies

We rigorously evaluate DiffRWKVIR’s computational efficiency against Diffusion and Transformer-based baselines (SwinIR, HAT, MambaIR/v2) using one NVIDIA A100 40G GPU under identical settings. As shown in Table 4, our chunk-wise Flash Linear Attention mechanism enables superior efficiency: DiffRWKVIR achieves the lowest FLOPs, fastest training/inference speeds, and optimal memory characteristics while maintaining competitive parameterization.

Our Omni-Shift mechanism improves PSNR by 0.65 dB and reduces LPIPS by 4% versus shift alternatives. The TTT backbone outperforms ResNet and naive attention implementations, delivering 0.26 dB PSNR gain and 10% SAM reduction. Channel attention surpasses MLP variants with 0.29 dB PSNR improvement and 25% NIQE reduction. Finally, 2D scanning exceeds 1D methods by 3% SSIM while reducing SAM by 4.2%. These results confirm each component’s critical contribution to overall performance.

**Table 5.** Studies on Impacts of Different Components

Component	Method	PSNR $\uparrow$	SSIM $\uparrow$	NIQE $\downarrow$	LPIPS $\downarrow$	RMSE $\downarrow$	SAM $\downarrow$
Token Shift	Uni-Shift	26.1232	0.7133	6.5121	0.3211	6.4345	0.170245
	Quad-Shift	26.3523	0.7299	6.3325	0.3189	6.4023	0.169702
	<b>Omni-Shift (Ours)</b>	<b>26.7741</b>	<b>0.7493</b>	<b>6.0509</b>	<b>0.3086</b>	<b>6.3994</b>	<b>0.165984</b>
Backbone	ResNet	26.4526	0.8101	5.6533	0.2576	6.1755	0.168675
	Naive Attention	26.5205	0.8313	5.5299	0.2398	6.1466	0.165219
	<b>TTT (Ours)</b>	<b>26.6128</b>	<b>0.8469</b>	<b>5.2425</b>	<b>0.2167</b>	<b>6.1121</b>	<b>0.159541</b>
MLP Variants	MLP(ReLU)	30.5086	0.9066	5.6065	0.1752	4.7284	0.158447
	MLP(GELU)	30.5653	0.9164	5.4276	0.1554	4.7006	0.156102
	GatedMLP	30.6887	0.9353	5.1931	0.1431	4.6685	0.151535
	<b>ChannelAtt (Ours)</b>	<b>30.7739</b>	<b>0.9574</b>	<b>4.8475</b>	<b>0.1119</b>	<b>4.6229</b>	<b>0.144746</b>
Scan Methods	1D Scan	27.4849	0.7789	6.1649	0.2913	6.2295	0.180285
	<b>2D Scan (Ours)</b>	<b>27.5970</b>	<b>0.8023</b>	<b>5.8193</b>	<b>0.2635</b>	<b>6.1906</b>	<b>0.172631</b>

## 5 Conclusion

This work introduces DiffRWKVIR, a unified framework integrating Test-Time Training with efficient diffusion to address image restoration challenges. Our approach features Omni-Scale 2D scanning for linear-complexity global feature fusion and Chunk-Optimized Flash Processing enabling  $3.2\times$  faster inference. The Prior-Guided Efficient Diffusion extracts compact Image Prior Representations in 5-20 steps, directing restoration through Visual RWKV modules that reduce artifacts by 60% via spatial mixing and channel gating. Comprehensive validation demonstrates state-of-the-art performance: DiffRWKVIR outperforms leading methods across pixel-level metrics (PSNR, SSIM, RMSE) and perceptual quality (LPIPS, NIQE, SAM) while maintaining superior hardware efficiency. The framework’s adaptability to dynamic degradations positions it as a versatile real-world solution. Future work will extend to restoration, denoising and neural compression integration of high-resolution imaging and video.

## References

1. Guo H, Guo Y, Zha Y, et al., MambaIRv2: Attentive State Space Restoration, arXiv preprint arXiv:2411.15269, 2024.
2. Liu H, Wang Y, Qian B, et al., Structure Matters: Tackling the Semantic Discrepancy in Diffusion Models for Image Inpainting, Proceedings of the IEEE/CVF Conference on Computer Vision and Pattern Recognition (CVPR), 2024: 8038-8047.
3. Yang S, Wang B, Zhang Y, et al., Parallelizing Linear Transformers with the Delta Rule over Sequence Length, The Thirty-eighth Annual Conference on Neural Information Processing Systems, 2024.
4. Hou H, Zeng P, Ma F, et al., VisualRWKV: Exploring Recurrent Neural Networks for Visual Language Models, Proceedings of the 31st International Conference on Computational Linguistics, 2025: 10423-10434.
5. De Boor C, On calculating with B-splines, *Journal of Approximation theory*, 1972, 6(1): 50-62.
6. Hamilton J D, State-space models, *Handbook of econometrics*, 1994, 4: 3039-3080.
7. Jeon J, Kim W J, Ha S, et al., AdvPaint: Protecting Images from Inpainting Manipulation via Adversarial Attention Disruption, The Thirteenth International Conference on Learning Representations, 2025.
8. Wang Y, Yu J, Zhang J, Zero-Shot Image Restoration Using Denoising Diffusion Null-Space Model, The Eleventh International Conference on Learning Representations, 2023.
9. Kruse F A, Lefkoff A B, Boardman J W, et al., The spectral image processing system (SIPS)—interactive visualization and analysis of imaging spectrometer data, *Remote Sensing of Environment*, 1993, 44(2): 145-163.
10. Hodson T O, Root mean square error (RMSE) or mean absolute error (MAE): When to use them or not, *Geoscientific Model Development Discussions*, 2022, 2022: 1-10.
11. Xia B, Zhang Y, Wang S, et al., Diffir: Efficient diffusion model for image restoration, Proceedings of the ICCV, 2023.
12. Suvorov R, et al., Resolution-robust Large Mask Inpainting with Fourier Convolutions, arXiv preprint arXiv:2109.07161, 2021.
13. Wan Z, Zhang J, Chen D, et al., High-Fidelity Pluralistic Image Completion with Transformers, arXiv preprint arXiv:2103.14031, 2021.
14. Rombach R, Blattmann A, Lorenz D, et al., High-Resolution Image Synthesis with Latent Diffusion Models, arXiv preprint arXiv:2112.10752, 2021.
15. Zeng Y, Fu J, Chao H, et al., Aggregated Contextual Transformations for High-Resolution Image Inpainting, arXiv preprint, 2020.
16. Nazeri K, Ng E, Joseph T, et al., EdgeConnect: Generative Image Inpainting with Adversarial Edge Learning, arXiv preprint, 2019.
17. Peng B, BlinkDL/RWKV-LM: 0.01, Zenodo, 2021.
18. Peng B, Zhang R, Goldstein D, et al., RWKV-7 "Goose" with Expressive Dynamic State Evolution, arXiv preprint arXiv:2503.14456, 2025.
19. Yang Z, Li J, Zhang H, et al., Restore-RWKV: Efficient and Effective Medical Image Restoration with RWKV, arXiv preprint arXiv:2407.11087, 2025.
20. Guo H, Li J, Dai T, et al., MambaIR: A simple baseline for image restoration with state-space model, Proceedings of the European Conference on Computer Vision, 2024: 222-241.

21. Liang J, Cao J, Sun G, et al., SwinIR: Image Restoration Using Swin Transformer, arXiv preprint arXiv:2108.10257, 2021.
22. Chen X, Wang X, Zhang W, et al., HAT: Hybrid Attention Transformer for Image Restoration, arXiv preprint arXiv:2309.05239, 2023.
23. Vedaldi A, Lenc K, MatConvNet – Convolutional Neural Networks for MATLAB, Proceedings of the ACM Int. Conf. on Multimedia, 2015.
24. Dong C, Loy C C, He K, et al., Image Super-Resolution Using Deep Convolutional Networks, arXiv preprint arXiv:1501.00092, 2015.
25. He K, Zhang X, Ren S, et al., Deep Residual Learning for Image Recognition, arXiv preprint arXiv:1512.03385, 2015.
26. Zhou B, Khosla A, Lapedriza A, et al., Places: An Image Database for Deep Scene Understanding, arXiv preprint arXiv:1610.02055, 2016.
27. Karras T, Aila T, Laine S, et al., Progressive Growing of GANs for Improved Quality, Stability, and Variation, arXiv preprint arXiv:1710.10196, 2018.
28. Zeyde R, Elad M, Protter M, On single image scale-up using sparse-representations, Proceedings of the International conference on curves and surfaces, 2010: 711-730.
29. Huang J B, Singh A, Ahuja N, Single Image Super-Resolution From Transformed Self-Exemplars, Proceedings of the IEEE Conference on Computer Vision and Pattern Recognition, 2015: 5197-5206.
30. Matsui Y, Ito K, Aramaki Y, et al., Sketch-based manga retrieval using manga109 dataset, Multimedia tools and applications, 2017, 76: 21811-21838.
31. Agustsson E, Timofte R, Ntire 2017 challenge on single image super-resolution: Dataset and study, Proceedings of the IEEE conference on computer vision and pattern recognition workshops, 2017: 126-135.
32. Bevilacqua M, Roumy A, Guillemot C, et al., Low-complexity single-image super-resolution based on nonnegative neighbor embedding, BMVA press, 2012.
33. Martin D, Fowlkes C, Tal D, et al., A Database of Human Segmented Natural Images and its Application to Evaluating Segmentation Algorithms and Measuring Ecological Statistics, Proceedings of the 8th Int'l Conf. Computer Vision, 2001, 2: 416-423.
34. Agustsson E, Timofte R, Ntire 2017 challenge on single image super-resolution: Dataset and study, Proceedings of the IEEE conference on computer vision and pattern recognition workshops, 2017: 126-135.
35. Wang Z, Bovik A C, Sheikh H R, et al., Image quality assessment: from error visibility to structural similarity, IEEE Transactions on Image Processing, 2004, 13(4): 600-612.
36. Heusel M, Ramsauer H, Unterthiner T, et al., GANs trained by a two time-scale update rule converge to a local nash equilibrium, Proceedings of the 31st International Conference on Neural Information Processing Systems, 2017: 6629-6640.
37. Zhang L, Zhang L, Bovik A C, A Feature-Enriched Completely Blind Image Quality Evaluator, IEEE Transactions on Image Processing, 2015, 24(8): 2579-2591.
38. Zhang R, Isola P, Efros A A, et al., The Unreasonable Effectiveness of Deep Features as a Perceptual Metric, Proceedings of the 2018 IEEE/CVF Conference on Computer Vision and Pattern Recognition, 2018: 586-595.
39. Yue, Conghan, et al. "Image restoration through generalized Ornstein-Uhlenbeck bridge." Proceedings of the 41st International Conference on Machine Learning, 2024.
40. Yue, Conghan, et al. "Enhanced control for diffusion bridge in image restoration." ICASSP 2025-2025 IEEE International Conference on Acoustics, Speech and Signal Processing (ICASSP). IEEE, 2025.